

Article

Study on Topology and Control Strategy of High-Precision and Wide-Range Hybrid Converter for Photovoltaic Cell Simulator

Jianfei Zhao ^{*}, Minqi Hua, Tingzhang Liu and Tao Yu

School of Mechatronic Engineering and Automation, Shanghai University, Baoshan District, Shanghai 200444, China; huamingqi@shu.edu.cn (M.H.); liutzh@staff.shu.edu.cn (T.L.); yutaotao@shu.edu.cn (T.Y.)

* Correspondence: jfzhao@shu.edu.cn; Tel.: +86-021-6613-0935

Received: 28 November 2018; Accepted: 20 December 2018; Published: 24 December 2018



Abstract: Aiming at the function and technical requirements of high-power photovoltaic cell simulation, high-performance programmable logic power supply and dc motor simulation, a high frequency isolation hybrid topology and control strategy based on current-source/voltage-source converter was studied and proposed. Firstly, according to the performance requirements of photovoltaic cell analog power supply, the control strategy requirements of the high-precision wide-range hybrid topology were proposed. Secondly, the working principle of the new hybrid topology was analyzed. At the same time, the equivalent model of the new hybrid topology was simplified and established, and the overall control strategy of the hybrid topology based on current compensation and sliding mode variable structure was proposed. Finally, simulation and experimental research on the hybrid topology was carried out, and the experimental test of photovoltaic cell simulation was completed. The simulation and experimental results show that the hybrid topology and control strategy proposed in this paper has the characteristics of wide-range output regulation, fast dynamic response, high efficiency and high power factor, and can be used for high performance photovoltaic cell simulation, programmable logic power supply and DC motor simulation.

Keywords: current source converter; voltage source converter; hybrid converter topology; sliding mode control; space vector control

1. Introduction

DC power supplies and load devices are core devices for energy conversion and diversified applications. They are widely used in various industries, from power adapters and switching power supplies to DC power transmission and distribution systems. High-performance, low-energy, energy-saving power supplies are important for efficient energy use. With the rapid development of power electronics and control technology, high-performance DC power supplies can be used as general-purpose power supplies such as DC system power supplies, communication base station power supplies, and experimental test power supplies. It can also be used as a photovoltaic analog power supply, a programmable power supply, a DC motor characteristic simulator, a special power supply, etc., which is receiving more and more attention.

In this study, the topology and control strategy of the above-mentioned high-performance DC power supply were taken as the research objectives; taking the photovoltaic battery analog power supply as a representative case, a high-precision wide-range hybrid topology and a control strategy are proposed to simulate the characteristics of photovoltaic cells under different environmental conditions. According to the technical requirements of actual photovoltaic cells, the designed topology should

have zero to open circuit voltage and zero to short circuit current, large capacity, high efficiency and power factor, high power density, fast dynamic response and low harmonic pollution, which are also the requirements of most high-performance DC power supplies. If the designed DC power energy can be fed back to the grid, the proposed topology can be extended to enable bidirectional flow of energy.

At present, high-performance high-power DC power supply is mainly based on the research of linear power supply and pulse width modulation (PWM) switching power supply. Due to its large size and low efficiency, the linear system loses energy on the power tube when it is used as a load, and fails to return energy to the power grid, which cannot meet the requirements of high power [1]. As a topology of high-power DC power supply and electronic load, PWM switching topology is a hot topic of current research. With the development of power electronics technology and control technology, voltage source PWM converter has been widely used in various fields, and research on control methods and modulation methods has emerged in an endless stream. Bai, H. et al. [2] and Karthikeyan, V. et al. [3] studied different control methods of high-performance power supply DC-DC converters. Bai, H. et al. [2] proposed a novel dual-phase-shift control strategy for a dual-active-bridge isolated bidirectional DC-DC converter to eliminate reactive power and increase system efficiency. Karthikeyan, V. et al. [3] proposed a varying phase angle control in isolated bidirectional dc-dc converter for integrating battery storage unit to a DC link in a standalone solar photovoltaic system. Zhao, C. et al. [4] and Tsang, K.M. et al. [5] innovated the topology of the voltage source DC-DC converter. Zhao, C. et al. [4] proposed an isolated three-port bidirectional DC-DC converter composed of three full-bridge cells and a high-frequency transformer, ensuring the minimum overall system losses. Tsang, K.M. et al. [5] implemented a fast-acting regenerative dc electronic load based on the single-ended primary inductor converter (SEPIC) converter.

In addition to the voltage source type converter, there is the current source one. At present, research on current source converters also receives great attention. The research content is mainly focused on control strategies, and most studies use current space vector control. Lopes, L.A.C. et al. [6] discussed the use of space vector modulation techniques to enhance the performance of a bidirectional three-SCR four-switch hybrid current source converter (HCSC). Gao, H. et al. [7] presented a model predictive switching pattern control for a current-source converter (CSC), which achieves superb low-order harmonics elimination performance in steady state and improved transient responses. Due to the overlap time causing negative influence in the output current waveform, Geng, Y. et al. [8] proposed overlap-time compensation method, which can effectively decrease the current harmonics introduced by the overlap time and improve the output current of the inverter. In the photovoltaic grid-connected application, current source inverters for detailed research have been used [9–11]. Chen, D. et al. [9] proposed a circuit topology of a single stage three-phase current-source photovoltaic grid-connected inverter with high voltage transmission ratio, which can suppress the energy storage switch's turn-off voltage spike. Rajeev, M. et al. [10] proposed a modified single-phase current source inverter with improved multi-loop control for photovoltaic interface application. Sun, Y. et al. [11] proposed a split-capacitor four-wire current source inverter, which is the dual of the split-capacitor four-wire voltage source inverter. In addition, the application of current source converters has gradually appeared in applications that were originally suitable for voltage source converters. For example, the following six articles respectively applied current source converters to micro-grid [12], wind turbine [13], multilevel converter [14], energy management in traction applications [15], indirect matrix converter [16] and permanent magnet synchronous motor drive [17]. It can be seen that the current source type converter has characteristics that make the control method and application research more and more in-depth and extensive.

When the voltage source converter is used as a controllable rectifier, the minimum output voltage on the DC side is close to the peak voltage on the AC side. Moreover, due to the existence of the control dead zone and the stable DC-DC optimal gain ratio requirement, the high-precision control of the low-voltage and small-current is basically impossible, and thus the field of the high-performance wide-range DC power supply is limited. Although the current source type PWM converter has a wide

range of DC voltage output, since the DC side current polarity cannot be changed, the power supply and load switching can only be realized by changing the voltage polarity, and its application range and occasion are also greatly limited. Therefore, based on the research of the current source converter topology, PWM pulse logic, modeling method and control strategy, a high-frequency isolation hybrid topology based on current-source/voltage-source converter is proposed in this paper. The current source type converter is controlled by the voltage space vector control method instead of the current space vector control method. On the basis of this, a hybrid topology overall control strategy based on current compensation and sliding mode variable structure is proposed, which has the advantages of being a high-capacity, high-precision, high-efficiency platform and a power factor platform of both current source converters and voltage source converters.

The organization of this paper is as follows. In Section 1, the topology and control requirements of high-precision wide-range power supplies based on the performance requirements of photovoltaic cell analog power supplies is discussed. In Section 2, a hybrid topology based on a current source converter is proposed and its working principle is analyzed. In Section 3, the equivalent model of hybrid topology is established, and the hybrid topology control strategy based on sliding mode variable structure and current compensation control is proposed and studied. In Section 4, the proposed hybrid topology and control strategy is simulated. In Section 5, the prototype design, the experimental study of hybrid topology and control, and the application test verification of photovoltaic cell simulation are presented. In Section 6, the paper is summarized.

2. Analysis of Topology and Control Strategy Requirements Based on Photovoltaic Cell Simulation

2.1. Photovoltaic Battery Model

A photovoltaic cell is an energy converter that converts solar energy directly into electrical energy. It is actually a DC power source that is affected by external factors such as light intensity and ambient temperature. In the absence of light, the basic behavior of a photovoltaic cell is similar to a normal diode. The equivalent circuit is shown in Figure 1.

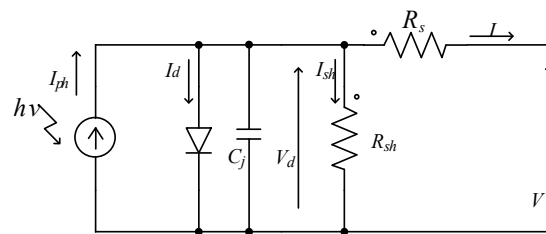


Figure 1. The equivalent circuit of photovoltaic cells.

I_{ph} is the photo-generated current, I_d is the dark current, R_s is the series resistance, R_{sh} is the bypass leakage resistance, and R_s and R_{sh} are the inherent resistance of the photovoltaic cells. Since the instantaneous response time of the device is negligible compared to the time constant of most photovoltaic systems, the capacitance C_j can be ignored in the analysis. R_s is usually small and has little effect on the system, so it is generally set to a fixed value. Therefore, the mathematical model is:

$$I = I_{ph} - I_d - \frac{V + R_s I}{R_{sh}} = I_{ph} - I_0 \left[e^{q(V + IR_s)/AKT} - 1 \right] - \frac{V + R_s I}{R_{sh}} \quad (1)$$

where I_0 is the diode reverse saturation current; A is the diode factor; T is the absolute temperature; q is the electron charge, 1.6×10^{-19} C; and K is the Boltzmann constant, 1.38×10^{-23} J/K.

Under ideal conditions, assuming that $R_{sh} \rightarrow \infty$, $R_s \rightarrow 0$, the photovoltaic cell current and voltage curve can be obtained according to Equation (1), as shown in Figure 2. The parameters of R_{sh} , I_{ph} , and I_0 are usually calculated by boundary conditions and setting conditions:

- (a) At the maximum power point: $V = V_{op}$, $I = I_{op}$.

- (b) Under the short circuit condition: $V = 0, I = I_{sc}$.
 (c) Under the open circuit condition: $I = 0, V = V_{oc}$.

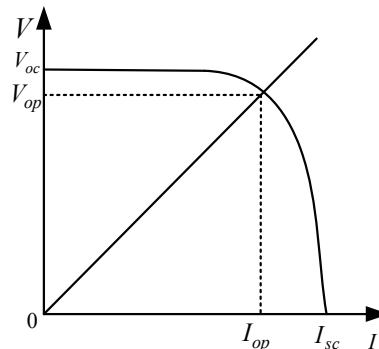


Figure 2. Photovoltaic cell output I-V curve.

V_{oc} is the open circuit voltage, I_{sc} is the short circuit current, V_{op} is the maximum power point voltage, and I_{op} is the maximum power point current. Substituting Condition (a) into Equation (1), Equation (2) can be derived.

$$R_{sh} = - \frac{V_{op} + R_s I_{op}}{\left(I_{ph} - I_{op} \right) - I_0 \cdot e^{q(V_{op} + I_{op} R_s) / AKT}} \quad (2)$$

When short-circuited, the diode reverse saturation current I_0 is much smaller than the short circuit current I_{sc} , thus it can be ignored. Therefore, using Condition (b), Equation (3) can be derived.

$$I_{ph} = \left(1 + \frac{R_s}{R_{sh}} \right) \cdot I_{sc} \quad (3)$$

Using Condition (c), Equation (4) can be derived.

$$I_0 = \frac{\left(I_{ph} - \frac{V_{oc}}{R_{sh}} \right)}{e^{qAKT \cdot V_{oc}}} \quad (4)$$

From Equations (2)–(4), R_{sh} , I_{ph} , and I_0 can be calculated, separately.

Equation (1) contains five parameters, I_0 , I_{ph} , R_{sh} , R_s and A , which are related to the light intensity, ambient temperature and the photovoltaic cell itself, and these five parameters are difficult to determine and are not convenient for engineering applications. Moreover, manufacturers of photovoltaic cells generally only provide users with standard test conditions, so the output characteristics of the photovoltaic cells under standard test conditions should be converted into mathematical models of photovoltaic cells under non-standard test conditions, thus solving the problem of calculation of output characteristics at arbitrary light intensity and temperature.

According to the research in [18–20], the mathematical model of engineering application of photovoltaic cells can be obtained as follows. The output characteristics of photovoltaic cells under standard test conditions is shown in Equation (5).

$$I = I_{sc} - C_1 I_{sc} \left(e^{\frac{V}{C_2 V_{oc}}} - 1 \right) \quad (5)$$

Among them: $C_1 = \left(1 - \frac{I_{op}}{I_{sc}} \right) e^{\left(-\frac{V_{op}}{C_2 V_{oc}} \right)}$, $C_2 = \left(\frac{V_{op}}{V_{oc}} \right) \left[\ln \left(1 - \frac{I_{op}}{I_{sc}} \right) \right]^{-1}$

The mathematical model of the photovoltaic cell under non-standard test conditions is shown in Equations (6) and (7).

$$\begin{cases} I_{scn} = I_{sc}(1 + a\Delta T) \frac{S}{S_{ref}} \\ I_{opn} = I_{op}(1 + a\Delta T) \frac{S}{S_{ref}} \end{cases} \quad (6)$$

$$\begin{cases} V_{ocn} = V_{oc}(1 - c\Delta T)(1 + b\Delta T) \\ V_{opn} = V_{op}(1 - c\Delta T)(1 + b\Delta T) \end{cases} \quad (7)$$

where $a = 0.0025 \text{ } ^\circ\text{C}$, $b = 0.5$, and $c = 0.00288 \text{ } ^\circ\text{C}$. I_{scn} , V_{ocn} , I_{opn} and V_{opn} under general working conditions are obtained to replace I_{sc} , V_{oc} , I_m and V_m under standard test conditions, and then the output characteristics of the photovoltaic cell under normal working conditions can be obtained by Equation (5), thereby solving the calculation problem of the output characteristics at arbitrary light intensity and temperature.

2.2. Topology and Control Strategy Requirements Analysis

From the output of the photovoltaic cell I-V curve and photovoltaic characteristics, the topology proposed in this paper should first have a high-precision wide-range requirement of output current from 0 to I_{sc} and output voltage from 0 to V_{oc} . From the mathematical model of photovoltaic cells under non-standard test conditions, the control strategy of the topology to be designed in this paper needs to be changed according to the light intensity and temperature change, that is, it has better fast dynamic tracking performance. In addition, when used as a multi-function power supply, the system often works at non-rated operating points. The designed hybrid topology also requires a high-efficiency and a high-power factor platform, which can save energy consumption and reduce reactive power under a variety of working conditions. In summary, the high-power analog power supply of photovoltaic cells represents the requirements of high-performance, high-precision, and high-response power supply in terms of function and performance, therefore this paper proposes a new hybrid topology and control strategy for power electronics to achieve the above requirements based on the simulation of high-power photovoltaic cells.

3. Hybrid Converter Topology

Usually, the high-power power supply for the wide output range of the rectifier often uses a voltage source type AC-DC and DC-DC two-stage converter topology. However, the three-phase voltage source AC-DC converter used in such a converter belongs to a boost converter, and the minimum voltage on the DC bus side is about the peak value of the AC grid line, and the voltage source converter has a dead zone during the control process. Even if a DC-DC is added, it is difficult to adjust the voltage in a wide range due to the limit voltage of the gain ratio. The current adjustment range is also the same, especially when both the voltage and the current are low. Therefore, this paper proposes a new hybrid converter topology based on current source converters to avoid the above problems. At the same time, through the design of the control strategy, the problem of unstable control and poor precision of the current source converter at low voltage and small current can be solved.

In view of the above analysis, a novel hybrid topology is proposed, which is composed of a current source type AC-DC converter, a current source type DC-AC converter, a high frequency transformer and a voltage source type AC-DC converter, as shown in Figure 3. In this paper, the three-phase AC voltage source is used as the main input power source for the solar cell model because the three-phase AC voltage source can achieve higher power and does not cause grid imbalance. CSCI is used in the first stage because the voltage source converter type cannot achieve a wide range of voltage and current variations from zero to maximum required for photovoltaic cell simulation. Since the current source converter current can only flow in one direction, to match CSCI, the second stage also uses a current source converter to ensure the circulation path. According to the characteristics of the current source type converter, the current can range from zero to the rated value, so the voltage can also be

adjusted in a wide range. Energy is absorbed from the three-phase grid to supply DC output. The path of energy flow flows from the three-phase grid through the LC filter into the three-phase current source converter (CSCI). The rectified energy passes through a current source type DC-AC converter (CSCII), a high frequency transformer (HFT), and a voltage source type AC-DC converter (VSCI) to output a DC with adjustable voltage and current.

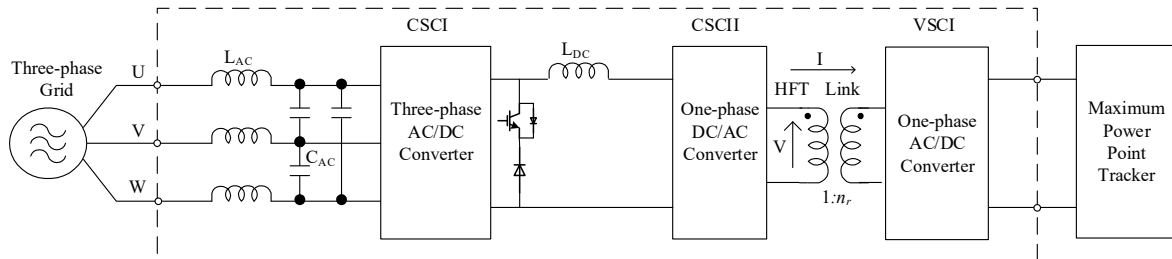


Figure 3. The proposed topology of the main circuit.

The specific working principle is shown in Figure 4. The three-phase AC-DC current source type converter ($S_{11}\sim S_{16}$) operates in the three-phase current source type PWM mode, and the current and voltage on the grid side are controlled in the same phase. The CSCII ($S_{21}\sim S_{24}$) on the primary side of the high-frequency transformer obtains a 50% duty cycle current source type PWM pulse. The current source type PWM requires that the upper and lower arms need to be overlapped, that is, simultaneously turned on to maintain the current path. The VSCI on the secondary side of the high-frequency transformer can be a half-bridge full-wave rectifier or a single-phase full-bridge rectifier. In this paper, a single-phase full-bridge diode rectifier is used. The circulation switch S_{17} is always in the ON state, and the freewheeling switching is automatically performed according to the ON and OFF states of S_{11} to S_{16} , thereby ensuring the circulation path and improving the efficiency. The energy is transmitted to the DC side via the AC-DC converter CSCI, the DC inductor L_{DC} , and the converter CSCII. The current flowing through the input side is: phase $U \rightarrow D_{11} \rightarrow S_{11} \rightarrow L_{DC} \rightarrow D_{21} \rightarrow S_{21} \rightarrow HFT \rightarrow D_{24} \rightarrow S_{24} \rightarrow D_{14} \rightarrow S_{14} \rightarrow$ phase V . The current flowing through the output side is: DC output side $N \rightarrow D_{34} \rightarrow HFT \rightarrow D_{31} \rightarrow$ Filter $L_{f1} \rightarrow$ DC output side P . Since the input and output sides are electrically isolated by a high-frequency transformer, in the case of high-power output, the output side can be connected in multiple stages in parallel to increase the output power.

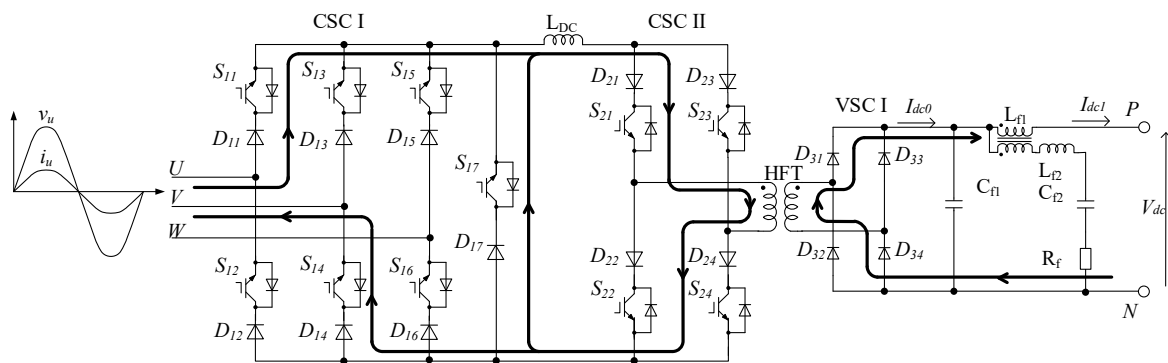


Figure 4. The principle and current flow of the main circuit.

If energy bidirectional flow is required, it is only necessary to replace the VSCI in the topology from a non-controllable diode rectifier to a controllable single-phase H-bridge, as shown in Figure 5. When energy is delivered from VSCI to CSCII, VSCI's S_{31} to S_{34} use a 50% duty cycle PWM pulse, while S_{21} to S_{24} use full conduction to rectify, allowing energy to flow in the opposite direction. When energy is delivered from CSCII to VSCI and CSCII, the S_{21} to S_{24} use a 50% duty cycle PWM pulse, the VSCI's S_{31} to S_{34} are all turned off, and the VSCI is equivalent to an uncontrolled rectifier

bridge composed of an IGBT freewheeling diode. The principle is the same as that shown in Figure 4. The energy bidirectional flow topology is suitable for applications such as battery charging and discharging, energy storage systems, and DC motor simulation. When used as a photovoltaic cell analog or general high-performance power supply, the uncontrollable rectifier bridge can be selected to reduce costs. The control method for the two-way flow of energy is introduced in Section 4, and verified in Section 5 by system simulation.

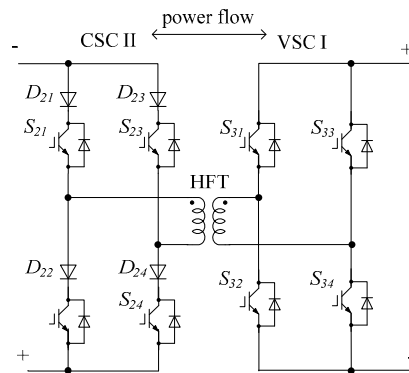


Figure 5. The DC/DC topology of the power bidirectional isolated circuit.

4. Hybrid Topology Control Strategy

4.1. Three-Phase Current Type PWM Pulse Logic

The three-phase current source type converter usually adopts current space vector control to divide the spatial angle into six regions, as shown in Figure 6a, in which any current vector will fall in one of the six regions. The vector can be generated equivalently to two adjacent current vectors and zero vectors.

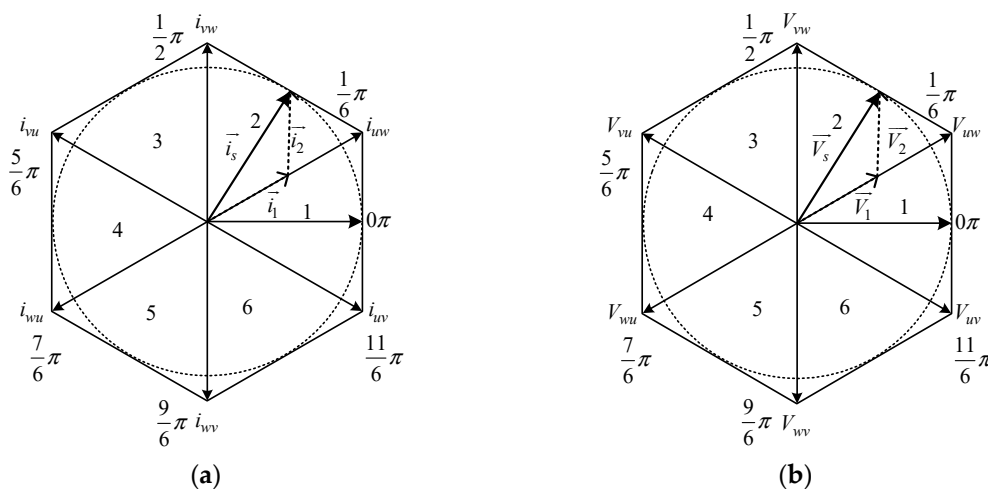


Figure 6. Space vector distribution: (a) current space vector; and (b) voltage space vector.

The calculation conditions for the ideal current source duty cycle are as follows:

- (1) The DC current is large enough, and the instantaneous DC current of the switch on/off is unchanged.
- (2) The DC current is continuous.

The formula for calculating the duty ratio is as follows:

$$m = \frac{i_s}{I_{DCL}} \tag{8}$$

where i_s is current vector value and I_{DCL} is current value of DC inductor L .

As can be seen from Equation (8), the present calculation method has the following problems. When the direct current is relatively small or the direct current is discontinuous, especially when it is close to zero, the calculation error of Equation (8) is relatively large, and the current control is likely to resonate. In addition, to measure the AC side current, two current sensors are required at the minimum. Since the DC inductance L is relatively small, the current will change when the switch is on/off, and a more stable and reliable calculation method needs to be designed.

According to the state of the AC side switch of the three-phase current source type PWM converter, it is known that the voltage on the AC side is applied to both ends of the DC inductor L . From the AC side, this voltage is based on the six voltage vectors generated by the AC switch. The current space vector shown in Figure 6a substantially coincides with the voltage vector shown in Figure 6b.

It can be seen from the analysis that:

- (1) The same as the generation of the arbitrary current vector of the interval, it is also possible to generate a voltage vector of an arbitrary interval.
- (2) According to the voltage vector, a voltage of any size on the DC side can be obtained.
- (3) According to the voltage on the DC side, instantaneous control of the DC side current can be performed. According to the control of the DC current, the control of the AC current is realized.
- (4) The phase control of the AC current is performed according to the phase of the AC voltage.

Therefore, instead of the current vector method, a duty ratio calculation method of controlling the instantaneous value of the DC inductance L current by an equivalent voltage vector can be employed. This method has many advantages. The instantaneous feedback control of inductance current on the dc side has a fast and stable response, which avoid divergence or inaccuracy control of Equation (8) caused by insufficient current accuracy or current interruption. When the voltage space vector is used, the denominator of the duty ratio of the load is calculated to be near the rated value, which improves the accuracy and reliability of the control.

To reduce harmonics and spike voltage, and improve the life and reliability of switching devices, the PWM also needs to find the optimal switching sequence during switching. In the process of switching, to generate the voltage space vector in the second region of $\pi/6$ to $\pi/2$, as shown in Figure 6b, switching of the voltage vectors V_1 and V_2 is performed. Figure 7a shows the current direction when voltage vector V_1 and V_2 are switched. Figure 7b,c illustrate the voltages V_{D11} and currents i_{D11} across D_{11} when V_1 is switched to V_2 in the two states of line voltage $V_{uv} > 0$ or $V_{uv} < 0$. The two cases are as follows:

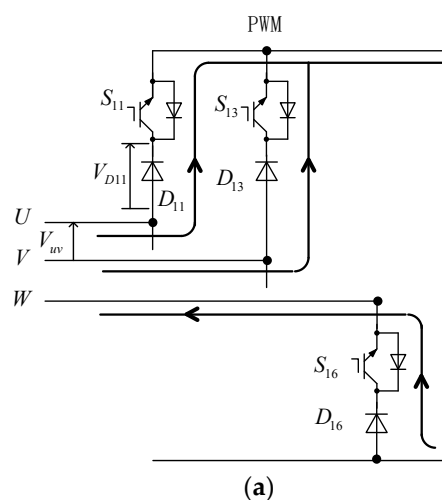


Figure 7. Cont.

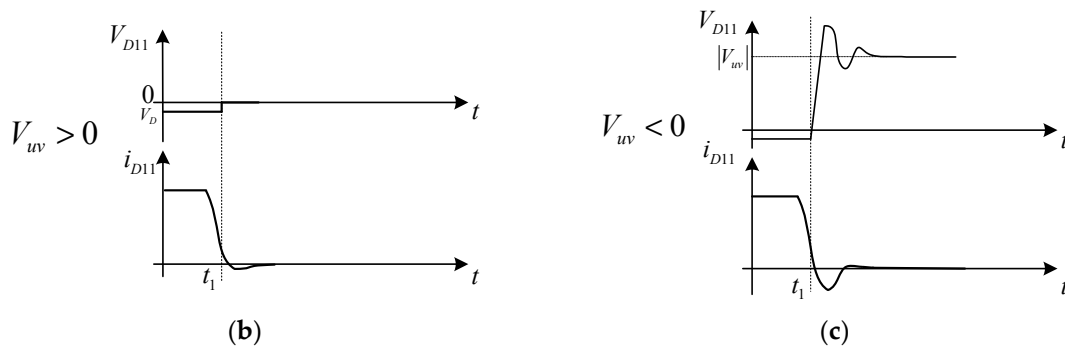


Figure 7. Current and voltage curves of D11 when V_1 changes to V_2 : (a) Schematic diagram of current direction when voltage vector V_1 and V_2 are switched; (b) Current and voltage curves of D11 when $V_{uv} > 0$; (c) Current and voltage curves of D11 when $V_{uv} < 0$.

As shown in Figure 7b, when $V_{uv} > 0$, and V_1 is switched to V_2 , since $V_{D11} < 0$, the spike voltage is relatively small. (Because V_{uv} is added at both ends of S_{11} , it is difficult to generate spike voltage.)

As shown in Figure 7c, when $V_{uv} < 0$, and V_1 is switched to V_2 , since $V_{D11} < 0$, the spike voltage is relatively large.

Therefore, to suppress the spike voltage, it is necessary to divide the same region into two small regions of $\pi/6$, and the vector voltages are sequentially switched according to the line voltage to suppress the spike voltage. In fact, the entire voltage space will be divided into 12 areas, for example:

In the second zone, when $V_{uv} > 0$ in the interval of $\pi/6$ to $\pi/3$, the order of switching is

$$\boxed{\rightarrow V_1 \rightarrow V_2 \rightarrow V_{w0}}$$

In the second zone, when $V_{uv} < 0$ in the interval of $\pi/3$ to $\pi/2$, the order of switching is

$$\boxed{\rightarrow V_2 \rightarrow V_1 \rightarrow V_{w0}}$$

To avoid the shock, the pulse overlap time of the current source type PWM should also be considered. The current source type switch is switched between “on” and “off”. To ensure continuous current, the current switch must be “off” after the next switch “on”. The time when the two switches are “on” together becomes the overlap time of the current source type PWM for the freewheeling of the current.

4.2. Hybrid Converter Equivalent Model and Control Strategy

According to the working principle of the topology, the hybrid topology can be equivalent. The equivalent model is shown in Figure 8, that is, the AC/DC current source type converter, DC inductor, and load, etc. constitute the basic buck circuit, among which the AC voltage is equivalent to the DC power supply V_s according to the PWM motion vector synthesis of the three-phase current-type converter switch tube, the load side is equivalent to the DC capacitor, S is equivalent to the six effective switching vector states of the three-phase current converter. Part D serves as a three-zero equivalent relationship with the six switches of the three-phase current source type converter, that is, the upper and lower tubes of the same bridge arm are simultaneously turned on, and can also be regarded as the equivalent relationship of the main circuit D_{17} and S_{17} freewheeling path. Therefore, the hybrid topology can control the DC inductor current i_L as the buck circuit.

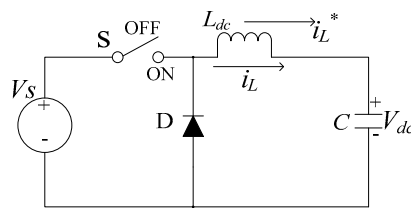


Figure 8. equivalent circuit of hybrid topology.

The relationship between the current of the DC inductor and the state of the switch is shown in Figure 9. To improve the response speed, the sliding mode variable structure is adopted to control the current.

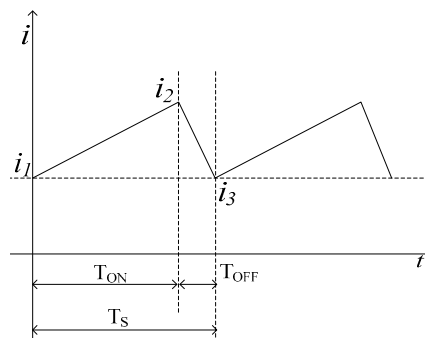


Figure 9. the relationship between the current of the inductor L_{DC} and the switching state.

When the switch is turned on, Equations (9)–(11) can be obtained.

$$V_s - V_{dc} = L_{DC} \frac{i_2 - i_1}{T_{ON}} \quad (9)$$

$$V_s = \frac{\sqrt{3}}{\sqrt{2}} V_{Line} \quad (10)$$

$$T_{ON} = T_S - T_{OFF} \quad (11)$$

where V_s is the equivalent voltage. When the switch is turned off, Equation (12) can be obtained.

$$-V_{dc} = L_{DC} \frac{i_3 - i_2}{T_{OFF}} \quad (12)$$

m is defined as the duty cycle and T_S is the switching period. If i_3 is given as the current reference value i^* , the i_1 tracking i^* can be realized by the sliding mode regulator controlling the duty ratio m . The current error e is defined as the state variable, and the state error equation can be expressed as

$$e = i^* - i_1 \quad (13)$$

The “chattering” phenomenon is suppressed by second-order sliding mode control, and the sliding surface is defined as:

$$s = e + k \int_0^t e dt \quad (14)$$

where k is the integral coefficient, which determines the convergence speed of the tracking error.

The exponential approach is chosen to design the sliding mode controller, i.e.,

$$\dot{s} = -\alpha s \operatorname{sgn}(s) - \beta s \quad \alpha > 0, \beta > 0 \quad (15)$$

The control rate is calculated and selected as follows,

$$m = \frac{V_S^*}{V_S} = \frac{V_{dc} + \Delta V_S^*}{V_S} = \frac{V_{dc} + k(i^* - i_1) - \alpha sgn s - \beta s}{V_S} \tag{16}$$

Sliding mode variable structure control has strong robustness and complete adaptability to system external interference and modeling dynamics, as well as advantages such as reduced order, decoupling, fast response, good dynamic characteristics, and easy implementation. Therefore, this paper uses sliding mode variable structure control to achieve the control of voltage variation. From the basic principle of the sliding mode variable structure, when the sliding surface and the control rate are selected, the sliding mode variable structure control system can be completely established.

According to the equivalent model, the control block diagram is shown in Figure 10, where i_{dc0} is the current that does not pass through the filter after the high-frequency transformer output is rectified, and i_{dc1} is the actual output value of the entire topology. i_{dc}^* is the expected output value of the entire topology. Their specific locations in the topology are shown in Figure 4. Since the secondary side of the high-frequency transformer has a filter, to improve the current control accuracy, the filter current needs to be compensated. Therefore, the PI control is added to compensate the capacitance current, and Δi_{dc} is the filter capacitor current compensation value. This paper controls the current i_{dc}^* equivalently by controlling the voltage v_{DC} across the L_{DC} . By introducing the feedforward amount V_{dc} , the system response time is reduced, that is, the expected output value of the entire topology i_{dc}^* is equivalently controlled by controlling the voltage variation Δv_s across the inductor. Since this paper obtains a high-precision and wide-range photovoltaic cell simulator by following the I-V curve of the photovoltaic cell with power electronics, it is necessary to give the illumination intensity and temperature parameters of the photovoltaic panel, and then the IV curve can be uniquely determined according to the i_{dc1} and V_{dc} of the load end, whereby the system can follow the output characteristics of the photovoltaic panel according to closed loop control. The I-V curves of photovoltaic panels at different light intensities and temperatures can be obtained from Equations (5)–(7).

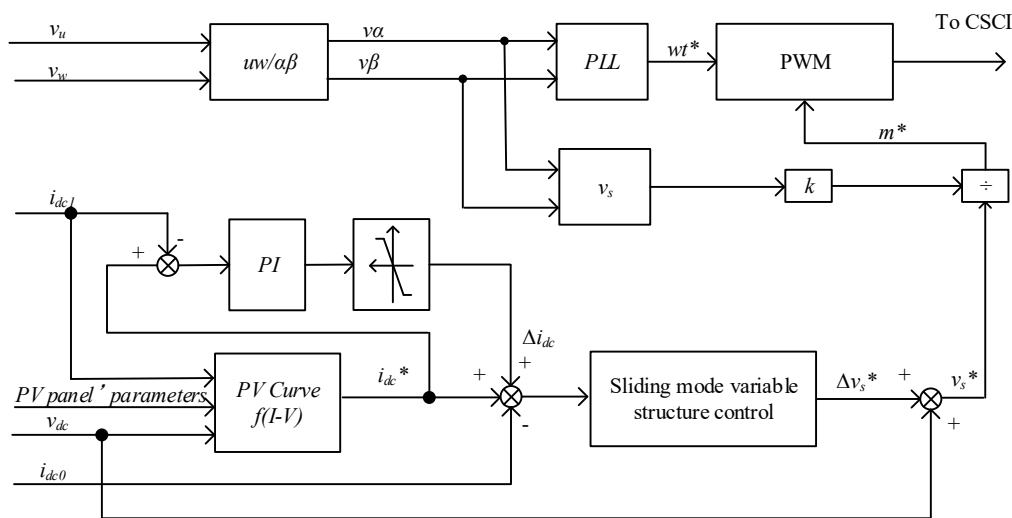


Figure 10. Block diagram of the overall control strategy.

If this topology is applied for battery simulation, electronic load, etc., the topological structure of high frequency transformer secondary side must be replaced for controlled single phase full bridge, as shown in Figure 5. In the control, only the S_{31} to S_{34} of the VSCI in the above control strategy adopt the 50% duty cycle PWM pulse, and the S_{21} to S_{24} adopts the full conduction mode to form the rectification, so that the opposite direction of energy flow can be realized.

5. Simulation Verification and Analysis

Combined with the analysis of hybrid topology and control strategy, considering the secondary side of the high-frequency transformer adopting the controllable single-phase full bridge, the wide-range photovoltaic simulation of this paper can be realized, and the reverse flow of energy can be realized to the grid. To make simulation verification more universal, the simulation verified the topology and control strategy with energy bidirectional flow. The circuit parameters were as follows: DC inductance, $L_{DC} = 0.25$ mH; AC filter capacitor, $C_u = C_v = C_w = 75$ μ F; and filter inductor, $L_u = L_v = L_w = 9.2$ mH. The simulation block diagram is shown in Figure 11.

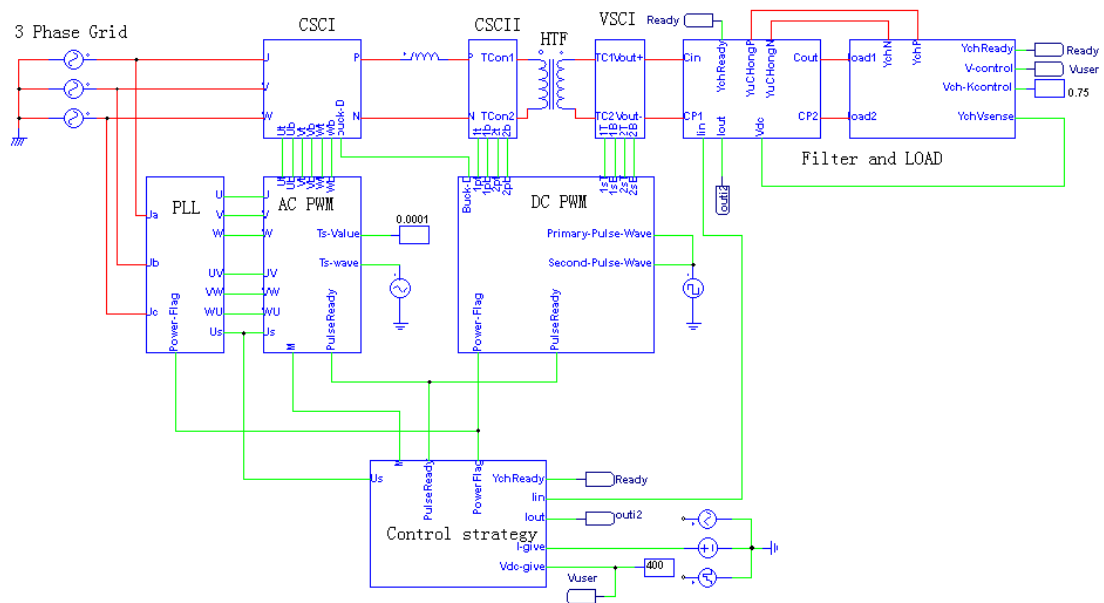


Figure 11. Simulation schematic diagram of DC hybrid bidirectional converter.

(1) Stable load verification

In Figure 12, I_{out2} is the DC side output current when the system is working as a power supply, I_{in2} is the DC side input current when the system is used as an electronic load, I_{ref} is the system given current, $PulseReady$ is the system opening operation signal, and v_u and i_u are u phase voltage and current on the grid side of the system. It can be seen in Figure 12a,b that the system startup sequence is valid and can be stably operated in a separate power and inverter mode for a given implementation.

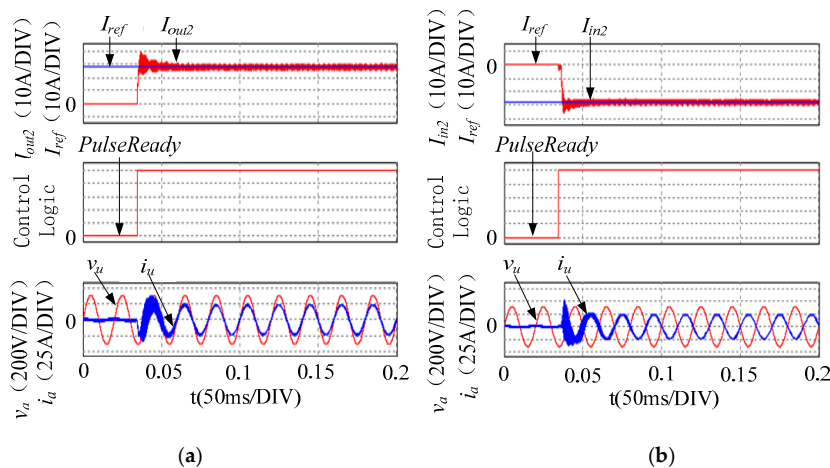


Figure 12. Waveforms in power and inverter mode: (a) waveform under power supply operation; (b) waveform under inverter condition.

(2) Dynamic tracking verification

In Figure 13, I_{dc} is the DC current of the system, I_{ref} is the given current of the system, and *PulseFlag* is the working signal of the different states of the system. As shown in Figure 13a, the system has fast tracking capability and bidirectional conversion function. It can perform mode conversion according to the given mode and can perform stably. As shown in Figure 13b, it can be concluded that the system has a fast dynamic response capability; even in the transient state of mode transformation, it still has a good response capability. As shown in Figure 13c, the system exhibits good homomorphic tracking and stability under different loads and different modes.

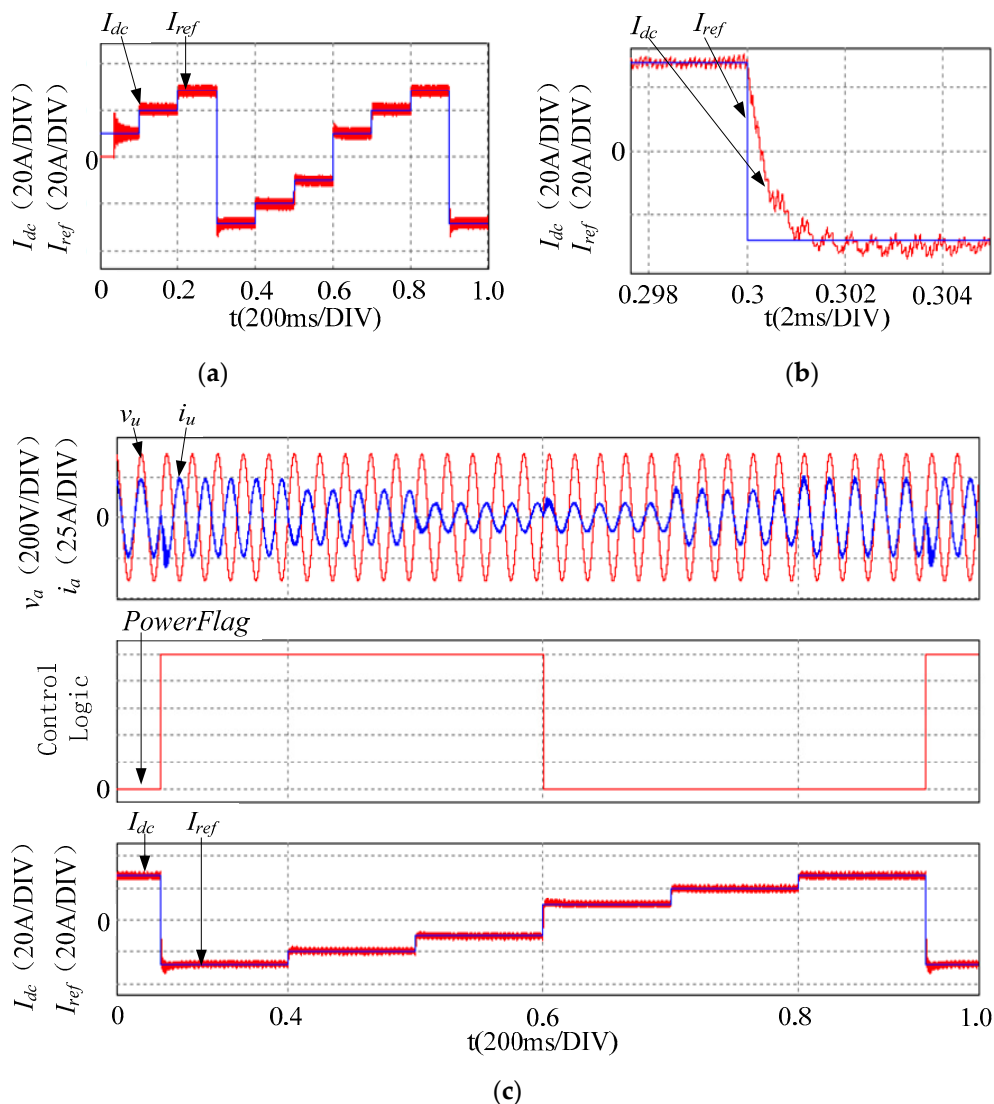


Figure 13. Dynamic Tracking Verification: (a) Tracking waveform of dynamic load; (b) Power supply and inverter step tracking waveform; (c) Dynamic runtime system waveform.

In summary, the simulation results verify the correctness of the proposed topology and control strategy. The simulation results show that the system has good control tracking performance and steady state performance in both stable and variable loads, and for the extended energy bidirectional flow function. It also has good control effects and meets the expected design requirements.

6. Experimental Analysis and Verification

According to the above topology structure and control strategy, a 10-kW experimental platform was designed. The specific structure is shown in Figure 14.

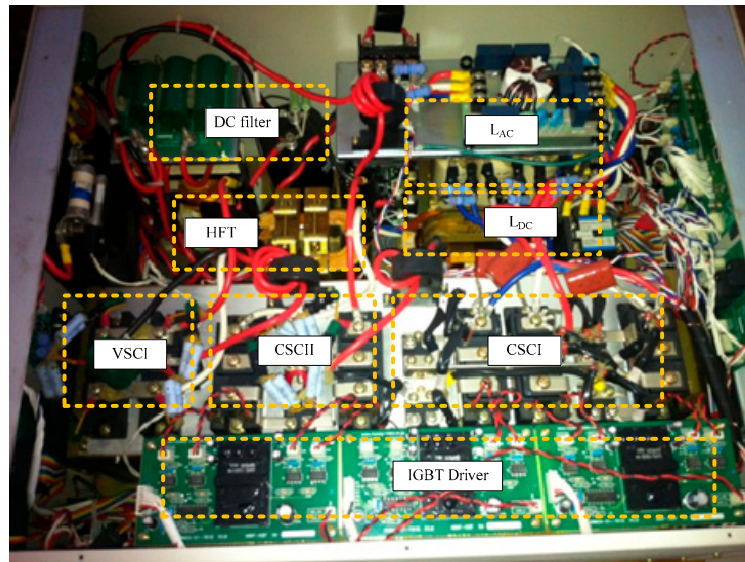


Figure 14. The 10-kW experimental platform.

6.1. Power Supply Experiment

Figure 15 shows the system test results when the DC output power was about 5 kW. The waveform was measured when the DC output voltage was 394.42 V and the DC output current was 12.795 A. The AC power factor was 1.0, the current THD was 3.37%, and the voltage THD was 0.81%. The system efficiency was 86.67%.

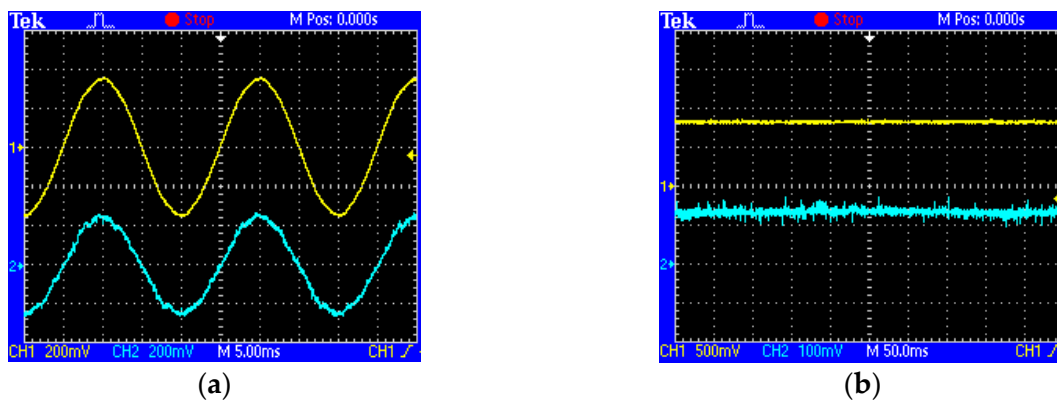


Figure 15. Hybrid topology 5 kW power mode waveform: (a) AC voltage (CH1: 100 V/200 mV); (b) DC voltage (CH1: 250 V/300 mV). AC current (CH2: 20 A/200 mV) DC current (CH2: 10 A/100 mV).

Figure 16 shows the system test results when the DC output power was about 10 kW. The measured waveform was measured when the DC output voltage was 393.82 V and the DC output current was 25.463 A. The AC power factor was 1.0, the current THD was 2.73%, and the voltage THD was 0.83%. The system efficiency was 85.27%.

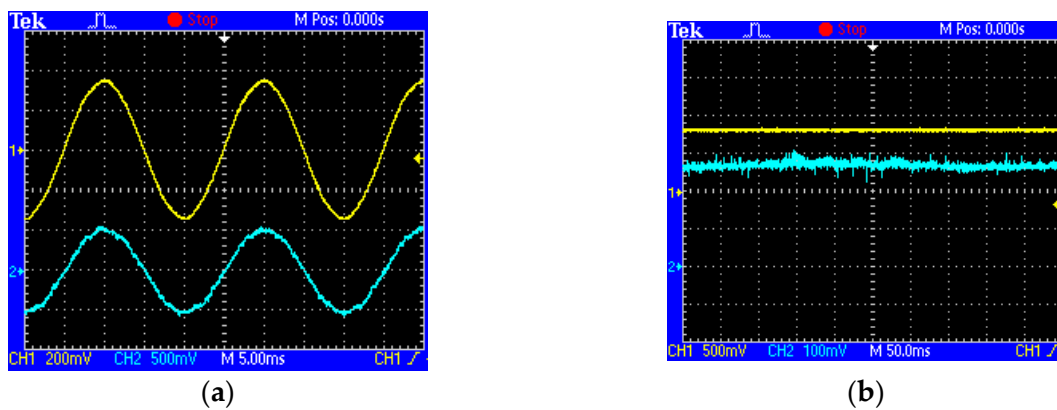


Figure 16. Hybrid topology 10 kW power mode waveform: (a) AC voltage (CH1: 100 V/200 mV); (b) DC voltage (CH1: 250 V/500 mV). AC current (CH2: 50 A/500 mV) DC current (CH2: 10 A/100 mV).

Finally, efficiency and power experiments were carried out for the system. The prototype was tested in the range of 0–10 kW of DC output power, and the power factor and overall efficiency of the grid side were tested. The experimental results are shown in Figure 17. It can be seen that the system output power was more than 85.27% in the range of 3–10 kW, and has a wide efficiency platform; the power factor of the system output power in the range of 2–10 kW was greater than 0.9924. Since the system often works at a non-rated operating point when used as a multi-function power supply, high-efficiency platforms and high-power factor platforms can save energy and reduce reactive power under various operating conditions. The efficiency of the power supply and the loss of the switching device are indeed two important research directions. For qualitative analysis, the current source converter is slightly less efficient than the voltage source converter under the same input voltage. In terms of efficiency optimization, although the topology proposed in this paper is not the most efficient at a single operating point, it can save energy and reduce reactive power under various operating conditions. In terms of switching loss, soft switching technology can be added according to the special needs of high power and high frequency occasions to reduce system losses.

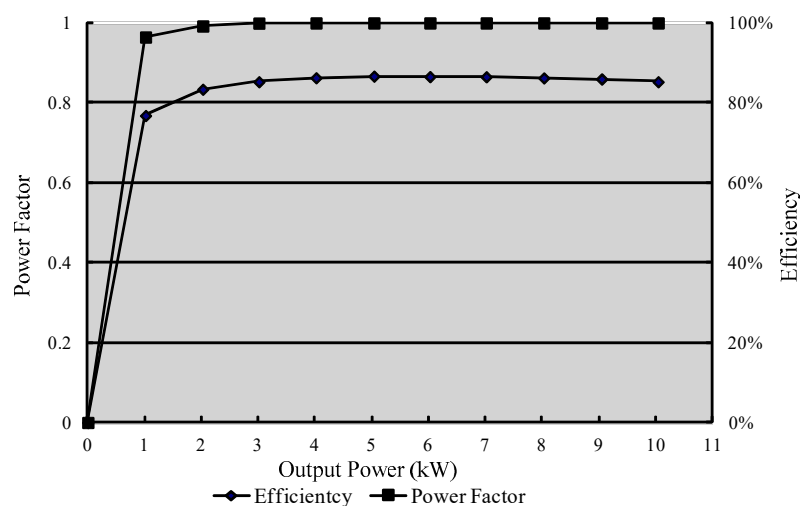


Figure 17. Efficiency and power factor curves of the proposed converter.

6.2. Power Supply Experiment

- (a) Design of solar cell characteristic curve Combined with the maximum capacity of the hardware of 10 kW, the characteristic parameters of the specified analog solar cell are as follows:
 Open circuit voltage V_{oc} : 368.1 V
 Short circuit current I_{sc} : 27.0 A

Maximum power point voltage V_{op} : 301.9 V

Maximum power point current I_{op} : 24.4 A

(b) Photoelectric dynamic input and tracking characteristics of photovoltaic cells

According to the photovoltaic simulation formula, the output characteristic curve of the photovoltaic cell at an illumination intensity of 1000 W/m^2 and a temperature of $25 \text{ }^\circ\text{C}$ is shown in Figure 18a. The designed output characteristic curve satisfies the specified characteristic parameters and curve characteristics. If the sunshine intensity changes within one day, as shown in Figure 18b, the upper position of the prototype changes the input of the PV panel parameters according to the change of the curve of Figure 18b, thereby obtaining the output characteristics of the photovoltaic cell simulation system, as shown in Figure 18c. The output characteristic curve of the photovoltaic cell is basically consistent with the sunshine intensity, which verifies the correctness of the solar cell output.

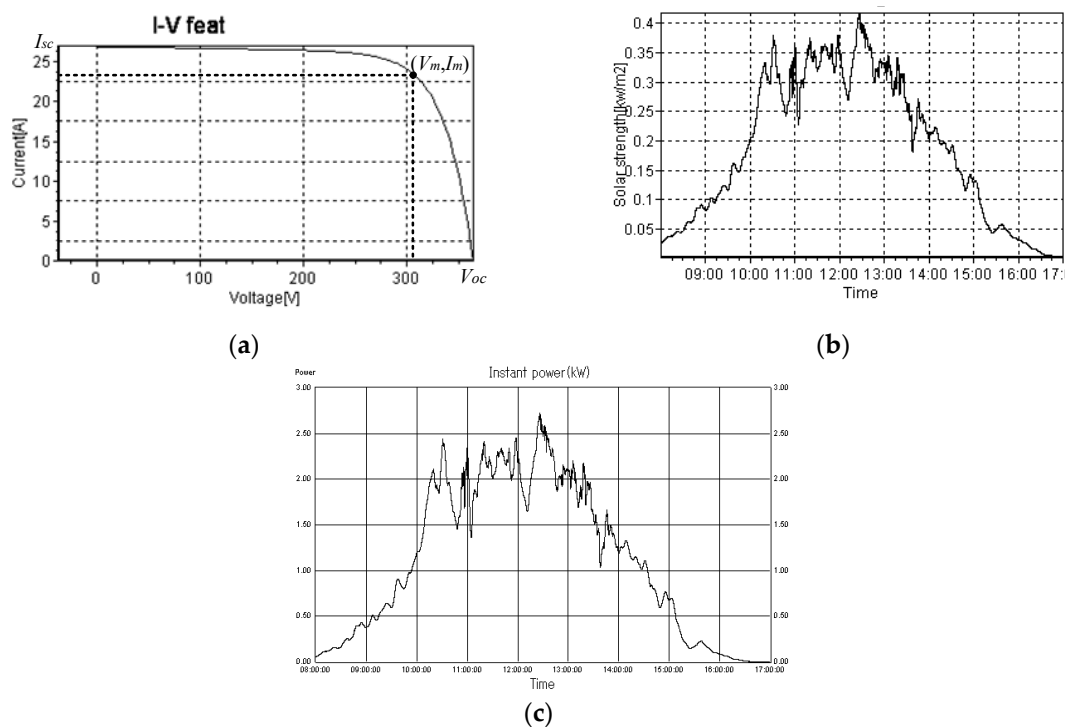


Figure 18. The feat curves and output of solar cells simulator: (a) I-V feat curve of solar cells; (b) feat curve of solar Strength on cloudy days; (c) The output of solar cells simulator.

A prototype based on the topology, control strategy and simulation method is proposed in the previous section. It was used as the photovoltaic simulator, and the output was connected with the photovoltaic grid-connected inverter with MPPT control. The test results are shown in Figure 19. It can be seen from the V-I feat window in Figure 19 that the V-I feat curve at the current operating point illumination intensity conforms to the standard characteristic waveform. The maximum power point of the actual output of the simulator and the calculated target maximum power point are substantially coincident, which demonstrates that the simulation and MPPT control results are correct. In the instant power window in Figure 19, the instantaneous output power indicated by the green line is the instantaneous power that the photovoltaic cell can theoretically output at different illumination intensities at different times, while the red line indicates the instantaneous power absorbed by the photovoltaic grid-connected inverter from the photovoltaic simulator using the proven MPPT control method. The two curves being basically the same represents that the photovoltaic simulator reaches the maximum power point and has the maximum power point characteristics of the photovoltaic cell. The yellow line represents the error of the two curves. During 40 min, the instantaneous power and maximum power point of the PV simulator change with time and illumination intensity. The whole

process realizes the simulation of the PV characteristics, which verifies the correctness and effectiveness of the topology and control methods presented in this paper.

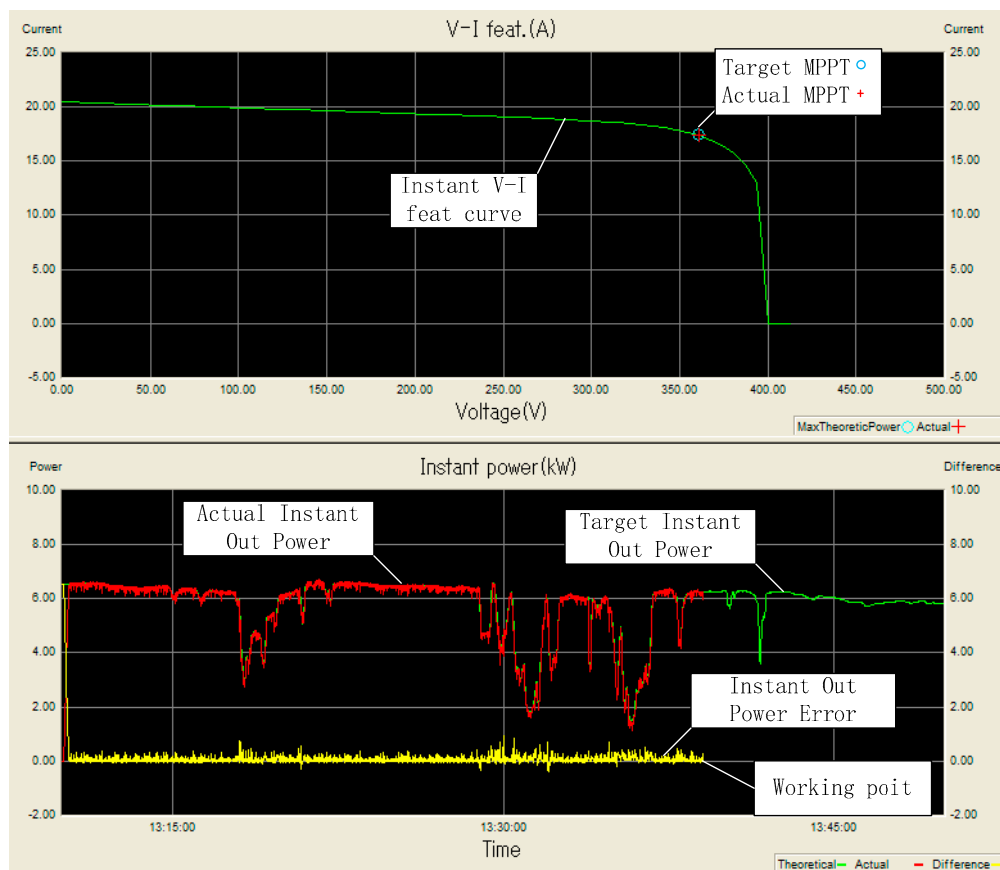


Figure 19. Photovoltaic cell V-I characteristic simulation and grid-connected comprehensive experiment.

7. Conclusions

Based on the large-capacity and wide-range photovoltaic cell simulation, first the requirements of photovoltaic cell simulation for power electronics topology and control strategy were analyzed, and then a new wide-range, wide-efficiency platform for power electronics hybrid converter topology was designed. The equivalent model is proposed by analyzing the working theory of hybrid topology. The current space vector was replaced by voltage space vector to control the current source converter. Based on the equivalent model, the overall control strategy with current compensation is proposed. Through theoretical analysis, simulation and experiment, the following conclusions are obtained:

1. Based on the hybrid topology of current source type converter, high frequency transformer and voltage source type converter, the voltage and current have a wide range of output functions, while the input and output high frequency isolation can expand capacity in parallel, which is suitable for high power and wide range of programmable power supplies, photovoltaic cell simulation, etc.
2. For the new hybrid topology, firstly, the voltage space vector was used to replace the current space vector control in the current source converter, which can solve the divergence problem when the small current or current is interrupted. Secondly, the capacitor current compensation control and the sliding mode variable structure control were used to improve the control accuracy and the speed of control. Finally, the new hybrid topology is equivalent to the basic Buck circuit model, which simplifies the control complexity and improves the control reliability.

3. The good characteristics of the proposed topology and control strategy under steady state and dynamics were verified by simulation. A 10 kW prototype was designed and verified by experiments. The experimental results show that the efficiency of the system exceeds 85% in the interval above 70%, the power factor exceeds 0.99 in the interval above 80%, and the total voltage harmonic distortion rate and total current harmonic distortion rate at the grid side are 0.83% and 2.73%, respectively, at the rated power, which satisfies the requirements of the grid for the equipment. Finally, a photovoltaic cell simulation experiment was carried out to realize the dynamic response under variable illumination intensity and the evaluation of output photovoltaic characteristics. The correctness and effectiveness of the photovoltaic cell simulation method were also verified.

In summary, this paper proposes a new hybrid topology, model and control strategy by taking photovoltaic cell simulation as an example, focusing on the single direction analysis and experimental verification of power supply. This paper also focuses on the topology expansion and simulation analysis of energy bidirectional flow. This topology and control method can be applied to battery simulation and electronic load applications through the expansion scheme described in this paper.

Author Contributions: Conceptualization, J.Z. and T.L.; methodology, J.Z.; software, M.H.; validation, J.Z., M.H., T.L. and T.Y.; formal analysis, J.Z. and M.H.; investigation, M.H. and T.Y.; resources, J.Z.; data curation, M.H. and T.Y.; writing—original draft preparation, J.Z. and T.Y.; writing—review and editing, J.Z. and M.H.; visualization, M.H.; supervision, T.L.; project administration, J.Z.; and funding acquisition, J.Z.

Funding: This paper and its related research were supported by grants from the Power Electronics Science and Education Development Program of Delta Environmental & Educational Foundation (DREG2016015).

Conflicts of Interest: The authors declare no conflict of interest.

References

1. Gong, G.; Ertl, H.; Kolar, J.W. Novel tracking power supply for linear power amplifiers. *IEEE Trans. Ind. Electron.* **2008**, *55*, 684–698. [[CrossRef](#)]
2. Bai, H.; Mi, C. Eliminate reactive power and increase system efficiency of isolated bidirectional dual-active-bridge DC–DC converters using novel dual-phase-shift control. *IEEE Trans. Power Electron.* **2008**, *23*, 2905–2914. [[CrossRef](#)]
3. Karthikeyan, V.; Gupta, R. Varying phase angle control in isolated bidirectional DC-DC converter for integrating battery storage and solar PV system in standalone mode. *IET Power Electron.* **2017**, *10*, 471–479. [[CrossRef](#)]
4. Zhao, C.; Round, S.D.; Kolar, J.W. An isolated three-port bidirectional DC-DC converter with decoupled power flow management. *IEEE Trans. Power Electron.* **2008**, *23*, 2443–2453. [[CrossRef](#)]
5. Tsang, K.M.; Chan, W.L. Fast acting regenerative DC electronic load based on a SEPIC converter. *IEEE Trans. Power Electron.* **2012**, *27*, 269–275. [[CrossRef](#)]
6. Lopes, L.A.C.; Naguib, M.F. Space-vector-modulated hybrid bidirectional current source converter. *IEEE Trans. Power Electron.* **2010**, *25*, 1055–1067. [[CrossRef](#)]
7. Gao, H.; Wu, B.; Xu, D.; Aguilera, R.P.; Acuna, P. Model predictive switching pattern control for current-source converters with space-vector-based selective harmonic elimination. *IEEE Trans. Power Electron.* **2017**, *32*, 6558–6569. [[CrossRef](#)]
8. Geng, Y.; Deng, R.; Dong, W.; Wang, K.; Liu, H.; Wu, X. An overlap-time compensation method for current-source space-vector PWM inverters. *IEEE Trans. Power Electron.* **2018**, *33*, 3192–3203. [[CrossRef](#)]
9. Chen, D.; Jiang, J.; Qiu, Y.; Zhang, J.; Huang, F. Single-stage three-phase current-source photovoltaic grid-connected inverter high voltage transmission ratio. *IEEE Trans. Power Electron.* **2017**, *32*, 7591–7601. [[CrossRef](#)]
10. Rajeev, M.; Agarwal, V. Single phase current source inverter with multi loop control for transformer-less grid-PV interface. *IEEE Trans. Ind. Appl.* **2018**, *PP*, 1–9.
11. Sun, Y.; Liu, Y.; Su, M.; Han, H.; Li, X.; Li, X. Topology and control of a split capacitor four wire current source inverter with leakage current suppression Capability. *IEEE Trans. Power Electron.* **2018**, *33*, 10803–10814. [[CrossRef](#)]

12. Gao, H.; Wu, B.; Xu, D. Nine-switch ac/ac current source converter for microgrid application with model predictive control. *IET Power Electron.* **2017**, *10*, 1759–1766. [[CrossRef](#)]
13. Rodríguez, A.; Huerta, F.; Bueno, E.J.; Rodríguez, F.J. Analysis and performance comparison of different power conditioning systems for SMES-based energy systems in wind turbines. *Energies* **2013**, *6*, 1527–1553. [[CrossRef](#)]
14. Ding, L.; Lian, Y.; Li, Y.W. Multilevel current source converters for high power medium voltage applications. *CES Trans. Electr. Mach. Syst.* **2017**, *1*, 306–314.
15. Garcia, J.; Garcia, P.; Capponi, F.G.; De Donato, G. Analysis, Modeling, and control of half-bridge current-source converter for energy management of supercapacitor modules in traction applications. *Energies* **2018**, *11*, 2239. [[CrossRef](#)]
16. Han, N.; Zhou, B.; Yu, J.; Qin, X.; Lei, J.; Yang, Y. A novel source current control strategy and its stability analysis for an indirect matrix converter. *IEEE Trans. Power Electron.* **2017**, *32*, 8181–8192. [[CrossRef](#)]
17. Zhang, Y.; Jahns, T.M. Uncontrolled generator operation of pm synchronous machine drive with current-source inverter using normally on switches. *IEEE Trans. Ind. Appl.* **2017**, *53*, 203–211. [[CrossRef](#)]
18. Degla, A.; Chikh, M.; Chouder, A.; Bouchafaa, F.; Taallah, A. Update battery model for photovoltaic application based on comparative analysis and parameter identification of lead-acid battery models behavior. *IET Renew. Power Gener.* **2018**, *12*, 484–493. [[CrossRef](#)]
19. Padhee, S.; Pati, U.C.; Mahapatra, K. Design of photovoltaic MPPT based charger for lead-acid batteries. In Proceedings of the International Conference on Emerging Technologies and Innovative Business Practices for the Transformation of Societies, Balaclava, Mauritius, 3–6 August 2016; pp. 351–356.
20. Khamis, A.; Mohamed, A.; Shareef, H.; Ayob, A.; Aras, M.S.M. Modelling and simulation of a single-phase grid connected using photovoltaic and battery based power generation. In Proceedings of the European Modelling Symposium, Manchester, UK, 20–22 November 2013; pp. 391–395.



© 2018 by the authors. Licensee MDPI, Basel, Switzerland. This article is an open access article distributed under the terms and conditions of the Creative Commons Attribution (CC BY) license (<http://creativecommons.org/licenses/by/4.0/>).